HHS Public Access

Author manuscript

Magn Reson Med. Author manuscript; available in PMC 2024 January 01.

Published in final edited form as:

Magn Reson Med. 2023 January ; 89(1): 177–191. doi:10.1002/mrm.29440.

Guanidinium and amide CEST mapping of human brain by high spectral resolution CEST at 3T

Kexin Wang[1,3], **Sooyeon Park**[1,4], **David Olayinka Kamson**[5], **Yuguo Li**[1,2], **Guanshu Liu**[1,2], **Jiadi Xu**[1,2]

[1.]F.M. Kirby Research Center for Functional Brain Imaging, Kennedy Krieger Research Institute, Baltimore, MD, USA

[2.]Russell H. Morgan Department of Radiology and Radiological Science, Johns Hopkins University School of Medicine, Baltimore, MD, USA

[3.]Department of Biomedical Engineering, Johns Hopkins University, Baltimore, MD, USA

[4.]Department of Neuroscience, Johns Hopkins University, Baltimore, MD, USA

[5.]The Sidney Kimmel Comprehensive Cancer Center at Johns Hopkins University, Baltimore, Maryland, USA

Abstract

Purpose: To extract guanidinium (Guan) and amide CEST on the human brain at 3T MRI with the high spectral resolution (HSR) CEST combined with the polynomial Lorentzian line-shape fitting (PLOF).

Method: Continuous wave (cw) Turbo Spin-Echo (TSE) CEST was implemented to obtain the optimum saturation parameters. Both Guan and amide CEST peaks were extracted and quantified using the PLOF method. The NMR spectra on the egg white phantoms were acquired to reveal the fitting range and the contributions to the amideCEST signal. Two types of CEST approaches, including cw gradient- and spin-echo (cwGRASE) and steady-state EPI (ssEPI), were implemented to acquire multi-slice HSR-CEST.

Results: GuanCEST can be extracted with the PLOF method at 3T, and the optimum B_1 = 0.6 μT was determined for GuanCEST in white matter (WM) and 1.0 μT in gray matter (GM). The optimum B_1=0.8-1 μT were found for amideCEST. AmideCEST is lower in both WM and GM collected with ssEPI compared to those by cwGRASE (ssEPI=(1.27~1.63)%; cwGRASE=(2.19~2.25)%). The coefficients of variation (COV) of the amide and Guan CEST in both WM and GM for ssEPI (COV: 28.6-33.4%) are significantly higher than those of cwGRASE (COV: 8.6-18.8%). Completely different WM/GM contrasts for Guan and amide CEST were observed between ssEPI and cwGRASE. The amideCEST was found to have originated from the unstructured amide protons as suggested by the NMR spectrum of the unfolded proteins in egg white.

Corresponding Author: Jiadi Xu, Ph.D., Kennedy Krieger Institute, Johns Hopkins University School of Medicine, 707 N. Broadway, Baltimore, MD, 21205, xuj@kennedykrieger.org, Tel: 443-923-9572, Fax: 443-923-9505.

Conclusion: Guan and amide CEST mapping can be achieved by the HSR-CEST at 3T combing with the PLOF method.

Keywords

chemical exchange saturation transfer (CEST); magnetization transfer contrast (MTC); guanidinium CEST; amide CEST; steady-state EPI (ssEPI); continuous wave gradient- and spin-echo (cwGRASE); polynomial Lorentzian line-shape fitting (PLOF)

INTRODUCTION

Protein concentration in the brain can be measured with the chemical exchange saturation transfer (CEST) MRI, which can significantly enhance the MRI sensitivity through the water signal (1–3). There are two commonly used CEST contrasts for protein mapping: amideCEST (or APT: amide proton transfer) (4,5) and guanidinium (Guan) CEST (6–8). AmideCEST is distinguished from the conventional APT-weighted MRI, which also focuses on the peak at 3.5 ppm, but is obtained by asymmetry analysis of the Z-spectrum and thus includes NOE and magnetization transfer contrast (MTC) effects (9,10). AmideCEST is the first CEST contrast discovered for protein mapping and has been intensively studied for decades (4,5). The extraction of the pure amideCEST from the brain Z-spectrum is challenging mainly due to the uncertainty of the amideCEST contribution in the crowded Z-spectrum. Instead of conventional asymmetry analyses, one relatively new strategy has been applied to acquire a full Z-spectrum with low saturation field strength B_1 and fit it by assuming a Lorentzian line-shape for each contributing signal, such as direct saturation (DS), guanidinium (Guan), amide, amine, and nuclear Overhauser effect (NOE) peaks (11–15). This method, however, still has interference from amide and aromatic NOE and other fast-exchanging amine and hydroxyl protons between 0 and 5 ppm, as summarized in the recent review (16). The extrapolated semisolid magnetization transfer reference (EMR) method further improved the Lorentzian fitting approach (17,18); nevertheless, it still faces the same issue as the Lorentzian fitting approach, i.e., mixed CEST signals are present due to the high saturation powers applied (17–19). Although the signals at 3.5 ppm extracted by the above three methods are mixed CEST contrasts, they can still be used for tissue protein profiling since all those CEST contrasts come from protein derivatives. That being said, we need to surpass the pH insensitive components such as NOE and MTC when probing pH changes in tissue, as demonstrated in several new comparative studies (20,21). In those applications where a more specific CEST contrast is needed, extracting the CEST contrast at a particular offset is highly desired. The crucial breakthroughs in determining the amideCEST contribution in the brain the Z-spectrum relied on the pH-dependent Z-spectra on protein phantom (22) and tissue homogenate (23), as well as Z-spectra on mouse stroke models (6,21,24–26). Notably, the recent deuterium-hydrogen exchanging studies on model proteins (22,27) discovered that the composite peak at 3.5 ppm in the protein Z-spectra includes a large portion of protons that exchange at very low rates. Those protons can still exchange with water through one relayed process similar to the aliphatic NOE(28–30), named amideNOE (22). Assisted by those discoveries, amideCEST was extracted from the crowded Z-spectrum and quantified using either a polynomial and Lorentzian line-shape fitting (PLOF) approach or a simplified principle of the three-point approach at both high

magnetic fields (24,25,31,32) and 3T (22). In the recent study on the human brain at 3T with the PLOF method, the amideCEST peak was assumed as a single peak at 3.5 ppm. Nonetheless, more careful inspection suggests that the amideCEST peak may have more sophisticated components (22).

Recently, an arginine guanidinium CEST (ArgCEST) signal was discovered in protein (6–8,22,26). This contrast has a detectable signal in the brain Z-spectrum because Arg is abundant in proteins (6% of all residues), and each Arg residue contains five side-chain exchangeable protons (four Guan protons and one NH group). AmideCEST and ArgCEST are among a few CEST contrasts that can be extracted with high confidence from the crowded *in vivo* Z-spectrum because of their low exchange rates (~60-70 Hz) (33). Since the mixed signal always complicates ArgCEST with creatine and phosphocreatine CEST (CrCEST/PCrCEST) at 2 ppm (16), the CEST peak at this range is named collectively named GuanCEST. Interestingly, GuanCEST is visible at the high field MRI (>7 T) on both animal (6–8,11,32) and human brains (15,23,34). It has not been observed on 3T MRI to our best knowledge. Recently, a study on rat brain at 4.7T clearly showed the feasibility of acquiring the GuanCEST peak at a low MRI field with high spectral resolution (HSR) CEST (26). This finding is further supported by one latest measurement of ArgCEST, in which the *in vivo* ArgCEST exchange rate was determined to be around 70 s^{-1} (33). The low exchange rate suggests the possibility of ArgCEST mapping at 3T. Inspired by the two discoveries, we acquire in this study the CEST signal with the HSR-CEST and extract the CEST peaks with the PLOF method in the human brain at 3T to find the detailed contributions to the amideCEST and to assess the possibility of GuanCEST mapping at 3T. We use the creatine phantom mixed with cross-linked bovine serum albumin (BSA) to find the optimum CEST saturation scheme and validate the PLOF fitting approach. Egg white phantoms are also used to confirm the origin of the amideCEST peak and the PLOF fitting range. Finally, two types of rapid CEST acquisition schemes, including continuous wave (cw) gradient- and spin-echo (GRASE) and steady-state EPI (ssEPI), are implemented and compared to achieve multi-slice HSR-CEST in a clinically feasible acquisition time.

METHODS

Phantom preparation

Egg white is an appropriate model to demonstrate the Guan and amide protons from mobile proteins (22). To demonstrate the NMR spectrum range of the folded and unfolded proteins, two egg white phantoms (100% liquid egg white) were prepared and titrated in NMR tubes to a pH value of 7.3. One of the egg white phantoms was mixed with 50% w/w urea to unfold the proteins, as urea upsets the established hydrogen-bonding pattern in proteins to trigger the loss of high-order protein structure (35–37). CEST was also used for mapping protein misfolding previously(38), which is different from the unfolding process by urea.

To examine the optimized B_1 values for the *in vivo* GuanCEST at 3T and assess the feasibility of fitting the MTC background utilizing the proposed PLOF method, a phantom with two 50 mL centrifuge tubes was prepared. One tube contained 50 mM Cr mixed with cross-linked BSA (15% w/w, CrCrossBSA), while another tube included the cross-linked BSA alone (15% w/w, CrossBSA). BSA was cross-linked using glutaraldehyde following

a previously described procedure (39). These two tubes were fixed in a brain-sized jar full of cross-linked BSA (15%). CrossBSA was utilized to mimic the strong background signal common to *in vivo* tissue. The recent study suggested a high concentration of GuanCEST in the brain (around 40 mM) (33); thus, a concentration of 50 mM Cr phantom was used for the optimization. The pH of the sample was titrated to 7.3, at which the Cr exchange rate was found to be around $45.3 \pm 0.9\ s^{-1}$ at room temperature (Supporting Information), which is close to the *in vivo* GuanCEST exchange rate reported recently (33). Overall, both the concentration and exchange rate of the Cr phantom are close to the in vivo protein GuanCEST; thus, it is a perfect model system to optimize our fitting procedure for *in vivo* GuanCEST.

NMR experiments

The NMR spectrum of egg white phantoms and the exchange rate measurement of the CrCrossBSA phantoms were performed on a Bruker 17.6T NMR spectrometer equipped with a triple resonance (TXI) NMR probe. Particularly, the NMR spectra for all phantoms were detected by a 3-9-19 WATER suppression by GrAdient Tailored Excitation (WATERGATE) sequence with a total echo time of 1 ms. The exchange rate was measured by the magnetization recovery of the exchangeable proton peaks after the inversion through a single selective Gaussian pulse (width of 2.5 ms), as detailed previously (33,40). The egg white NMR spectra were collected at 37 °C. Additionally, the exchange rate of the CrCEST in the CrCrossBSA phantom was measured at 21 °C. There is no water or air heater equipped on the human scanners. Therefore, the MRI experiments of the CrCrossBSA phantom with the 3T human scanner have to be performed at room temperature, i.e., 21 °C. In order to match the temperature used for the MRI experiments, the NMR exchange rate measurement was also performed at room temperature. The exchange rate measurement with NMR is reported in the Supporting Information.

MRI experiments

All human and phantom scans were acquired on a Philips MR Ingenia Elition 3.0T (Philips Healthcare, Best, The Netherlands) using a quadrature transmit body coil and a 32-channel phased-array receive head coil (Philips Healthcare, Best, The Netherlands). Human studies were approved by the Johns Hopkins Medicine IRB and were performed on 15 healthy subjects (22–63 years old), all of whom provided informed consent. Two pads were placed close to the temporal lobe on each side of the head to minimize head movement during the study.

A cw saturation scheme provides a high labeling efficiency (41). When performing CEST with multi-slice Turbo Spin-Echo (TSE) acquisition, the MTC from the neighboring slices can also interference with the CEST signal (42). Therefore, a single slice cw TSE (cwTSE) sequence (Fig. 1a) was used to optimize the B_1 value and serve as a reference for determining the labeling efficiency of other CEST sequences. The duration of the cw saturation was fixed at 1 s. The TSE readout parameters were TE/TR = 5.6 ms/3.5 s, refocusing angle = 120°, TSE factor = 37, FOV = 220 × 220 mm^2, space resolution = 3 × 3 × 5 mm^3. The image matrix was resized to 96 × 96 during reconstruction. Seven B_1 values (0.3, 0.4, 0.6, 0.8, 1.0, 1.2, 1.5 μT) were collected. A total of 69 saturation offsets

were swept from ranges 8.0 to −2.2ppm every 0.2 ppm except for the ranges 1.1 to 4.0 ppm which were measured every 0.1 ppm. The full frequency offsets are listed in the Supporting Information following the scan order. The unsaturated reference (M_0) was acquired with the same sequence at a saturation offset of 200 ppm. The total scan time for each cwTSE method was 4 min 5 s with 3.5 s for each offset. The cwTSE method was also used in the study of the CrCrossBSA and CrossBSA phantoms with identical CEST saturation and acquisition parameters except for eight B_1 values (0.2, 0.3, 0.4, 0.6, 0.8, 1.0, 1.2, 1.5 μT).

Since many saturation offsets (a total 69) collected in the HSR-CEST resulted in extended total scan time, rapid multi-slice CEST methods that shorten the total scan time were critical for future clinical applications. In our study, we compared two types of fast-acquisition MRI methods: 3D GRASE with cw saturation (cwGRASE) (Fig. 1b) (43) and steady-state EPI (ssEPI) (Fig. 1c) (44,45). Although TSE method was commonly used for single slice CEST study, the acquisition time is usually too long for 3D acquisition (22) unless advanced acquisition strategies are used (46). The geometries in the 3D/multi-slice MRIs were identical to the cwTSE method; however, 13 slices were collected in each 3D/multi-slice method. Before the CEST experiments, the first-order pencil beam (PB)-volume shimming method was applied to the image slices. The Guan and amideCEST contrasts and overall SNR for the MRI methods were compared. In the cwGRASE, 0.95 s saturation length and 0.8 μT were used. 3D GRASE MRI readout (2 shots) was utilized with TR/TE = 3 s/13 ms, EPI factor = 13, TSE factor = 13, SENSE = 2 in the AP direction, and the total GRASE readout was 169 ms. The total scan time for cwGRASE was 7 min, i.e., 6 s for each offset. For the ssEPI method, multi-shot EPI (EPI factor = 17) using 50 ms sinc-Gauss saturation pulses with a square-root B_1 of 0.8 μT. Other parameters included TR/TE = 1326/6.9 ms and a readout flip angle of 10°. A mixing time of τ_{mix} =14 ms was used. The total scan time for the ssEPI was 6 min with 5.2 s for each offset. For both swGRASE and ssEPI methods, FOV = 220 × 220 mm^2, space resolution = 3 × 3 × 5 mm^3 were implemented. The image matrix was resized to 96 × 96 during reconstruction.

T_1 maps, acquired by a look-locker sequence with geometry identical to the CEST scan, were used as the reference for the segmentation of gray matter (GM) and white matter (WM). Additionally, these maps provided T_1 mean value for the PLOF fitting method. In detail, 38 images were acquired with TR/TE = 2.3/1.2 ms and a readout flip angle of 4°. Pixel-by-pixel fitting was performed on a three-parameter model $(A - Be^{-\frac{TI}{T_1^*}})$ to obtain T_1 (as $T_1 = (B/A - 1)T_1^*$) (47).

Motion correction

Since the scan time of either cwGRASE or ssEPI was more than 5 minutes, brain motion was unavoidable even with two pads; therefore, we carried out motion correction on the images of these two methods for each subject. Due to the characteristic contrast of CEST and our interest in Guan and amide signal, we set the images at 3.3 ppm as the fixed (48) in the motion correction function of Advanced Normalization Tools (ANTs)(49) and registered all the other images to it. 3D rigid-body motion model was assumed at a gradient step of 0.005, with the metric of global correlation randomly sampled across 50% of the pixels.

Data Analysis

All MRI images were processed using custom-written MATLAB scripts (MathWorks, www.mathworks.com). Both Guan and amideCEST signals were extracted simultaneously with the PLOF method described previously (16,22,31) and are detailed in the Supporting Information. The SNR of the images was calculated by the mean values in the signal regions divided by the standard derivation of the noise background at four image corners, each of which is 16 × 16 pixels.

RESULTS

NMR spectra of egg white phantoms

The NMR spectra of egg white phantoms with and without 50% urea are plotted in Fig. 2. The downfield protein NMR peaks locate between 1.5 to 5 ppm for the untreated egg white. Once the egg white was treated with 50% urea, the amide peaks formed a sharp single peak centered at 3.5 ppm and a narrow frequency range of 3-4 ppm. Furthermore, the side-chain amides from asparagine (Asn) and glutamine (Gln) were converted to sharp doublet peaks separated by around 0.7 ppm due to the slow interconversion of two possible configurations (50–52). The assignment of the Arg side chain Guan protons was assigned based on the chemical shift determined by other proteins. (50–53) Therefore, the fitting range for the PLOF fitting method was set to 1.5 to 5.0 ppm in the following *in vivo* studies. This fitting range was further supported by the downfield MRS spectrum recorded on the human brain at 3T (54).

CrCrossBSA Phantom validation

The B_1-dependence of the Z-spectra of CrCrossBSA and CrossBSA are plotted in Fig. 3a. A broad Z-spectral background is observed for both the CrossBSA and CrCrossBSA phantoms (Fig. 3a), with the Z-spectra overlapping over most of the frequency range except between 1 ppm to 3 ppm, where a single peak from the Cr is found. Subtracting the Z-spectra from CrossBSA with and without Cr in Fig. 3a results in the pure Cr Z-spectra (Fig. 3b). A sharp Cr peak centered at 1.9 ppm is observed for all B_1 values (0.2 μT to 1.5 μT). The MTC background is also perfectly fitted with the PLOF function proposed in Eq. S3 (R^2>0.99) as validated on the Z-spectra from the CrossBSA phantom (Fig. 3c). The fitting range is identical to those applied for the following human brain studies, i.e., [1.5, 5.0] (ppm) was excluded for the background fitting. The B_1-dependent CrCEST signal (Fig. 3d) peaked at B_1 = 0.6 μT. The ground truth CrCEST signal was extracted by the differential Z-spectra at Fig. 3b. When B_1 increases from 0.2 to 0.6 μT, the CrCEST signal increases due to the higher labeling efficiency. However, it drops at further higher B_1 values. In order to further validate the PLOF method in extracting CrCEST signal, the CrCEST extracted with the PLOF method on the Z-spectra of CrCrossBSA alone is plotted and compared with the ground truth CrCEST (Fig. 3d). The two methods perfectly match each other with a maximum difference of 0.73%. The differences were computed across all B_1 values, and the maximum difference was found at B_1=1.5 μT. The small differences indicate that the the PLOF method proposed here can reliably extract CrCEST signal with strong MTC present.

Extraction of Guan and amideCEST in the human brain

The PLOF background fitting and the B_1 optimization for the Guan and amideCEST on the human brain at 3T are illustrated in Fig. 4. The T_1-based mask separated WM and GM with a cut-off value of 0.7 s and the boundary of 0.5~1.0 s, as demonstrated in Figs. 4a and b. Since cwTSE is recognized as a standard protocol for CEST, the demonstration and optimization are performed with this specific method. Typical Z-spectra between 0.5 ppm and 6.7 ppm for the human brain recorded using cwTSE as a function of B_1 are depicted in Figs. 4c, d for GM and WM, respectively. The separation of the WM/GM in the brain is not only used for finding the optimization B_1 value but also used to demonstrate the WM/GM CEST contrast with different B_1 values. The MTC background of WM is stronger than that of GM, i.e., GM absolute Z-values are higher than WM, which is consistent with conventional MTC studies (55). CEST signals are clearly observed between 0.5 and 5 ppm for both WM and GM Z-spectra with B_1 values < 1.2 μT. In order to illustrate the process of extracting the Guan and amideCEST signal with the PLOF method, the PLOF fitting curves for the background Z_{back} with Eq.S3 are plotted in the same figures (Figs. 4c, d). The background can be well fitted with four parameters in Eq. S3 for the whole 0.5-8.0 ppm. The difference spectra between the Z-spectra and the background Z_{back}, i.e., ΔZ spectra, are plotted in Figs. 4e, f for GM and WM, respectively. There are two prominent peaks in all ΔZ spectra with B_1< 1.0 μT, representing the signals from amide (~3.5 ppm) and Guan (~2.28 ppm). With high B_1 values such as 1.5 μT, the GuanCEST peak rapidly decreases, particularly in the WM. The resulting B_1-dependent Guan and amideCEST signals are shown in Fig. 4g and demonstrate the different B_1 dependence for WM and GM. The optimum B_1 value for the Guan and amideCEST in the GM is 1 μT, while in the WM, the optimum B_1=0.6 μT for GuanCEST and B_1=0.8 μT for the amideCEST. Therefore, the B_1 (cw CEST) or square-root B_1 (pulsed CEST) was set to 0.8 μT in the following Guan and amideCEST studies. The accurate offset range of the CEST peaks in the human brain can be obtained with lower B_1 values, as seen from Eq. S5 (<0.5 μT). The ΔZ-spectrum from GM is plotted in Fig. 4h together with the NMR spectrum of the egg white phantom mixed with 50% urea. The frequency range of the amideCEST perfectly matches with the unfolded egg white, i.e., 3.0-4.0 ppm.

The typical GM and WM Z-spectra, together with the PLOF fitting results are demonstrated in Fig. 5 at the range of 0.5~8.0 ppm from the whole GM and WM ROIs (Figs. 4a and b), respectively. To further illustrate the Guan and amide CEST extraction and quantification, the ΔZ-spectra, including the two individual peaks (Guan and amideCEST) and the sum of the two peaks, are shown for GM (Fig. 5b) and WM (Fig. 5c), respectively. The ΔZ-spectrum can be perfectly fitted with the two CEST peaks (R^2 > 0.9998) with center offsets of 2.28±0.04 and 3.50±0.03 ppm were determined for Guan and amideCEST, respectively.

Comparison of rapid CEST acquisition methods

The whole brain images (M_0 images) acquired with the 3D cwGRASE and multi-slice ssEPI are plotted in Figs. 6a, b with their SNR comparison with cwTSE (Fig. 6c). Overall, the cwGRASE images exhibited fair image quality with some minor artifacts, and a strong CSF signal was observed due to the long acquisition time (169 ms) (Fig.6a). The image quality obtained by ssEPI is much better than those from cwGRASE, judging from the clear contrast

between WM/GM. The ssEPI SNR values were close to those of cwGRASE images (ssEPI vs. cwGRASE: 737±379 vs. 602±327; p=0.083), while the SNR of cwGRASE was much higher than that of cwTSE (cwTSE vs. cwGRASE: 280±99 vs. 602±327; p=0.03) (Fig. 6c). Furthermore, the SNR is homogeneous across all the slices for the ssEPI, while the SNR varies significantly across the slices for the cwGRASE method (Fig. 6d).

The Guan and amideCEST maps obtained with the PLOF method are visualized in Figs. 7a and b for the cwGRASE and ssEPI methods, respectively. Overall, there are low contrasts in the Guan and amideCEST maps across the whole brain acquired with cwGRASE (Fig. 7a). On the other hand, much stronger WM/GM contrasts were observed for both Guan and amideCEST maps collected with ssEPI (Fig. 7b). This contrast can be well observed with the zoomed images in Figs. 7c and d. The single-slice Guan and amideCEST maps for all subjects demonstrate that cwGRASE offers much better reproductivity than the ssEPI method. In order to quantify the Guan and amideCEST values, Figure 8a shows the averaged Guan and amideCEST values in WM and GM for all subjects recorded with cwTSE (n=6), cwGRASE (n=6), and ssEPI (n=6). The regions of interest for GM and WM were extracted from the T_1 maps as demonstrated in Figs. 4a and b. The mean and standard deviation of the Guan and amideCEST signals in GM/WM are listed in table 1 and plotted in Figs. 8a and b. For both amide and GuanCEST, the WM and GM signals are comparable between cwTSE and cwGRASE methods

When comparing the amide and GuanCEST acquired with cwGRASE and ssEPI, amideCEST is lower in both WM and GM collected with ssEPI compared to those by cwGRASE (ssEPI=(1.27~1.63)%; cwGRASE=(2.19~2.25)%), while the obtained GuanCEST is similar between ssEPI and cwGRASE methods (ssEPI=(0.93~1.25)%; cwGRASE=(1.22~1.43)%). However, the coefficients of variations (COVs) of amide and Guan CEST in both WM and GM for ssEPI (amide COV: 28.6-32.0%; Guan COV:33.1-33.4%) are significantly higher than those of cwGRASE (amide COV: 10.0-10.3%; Guan COV: 8.6-18.8%;) (Figs. 8a–b). This is consistent with the observation on the amide and Guan CEST maps for all subjects (Figs. 7 e and f). Overall, both cwGRASE and ssEPI can provide uniform contrast across the whole brain, as seen from the Guan and amideCEST contrasts for each slice in Figs. 8c–f. The typical single slice MTC background at 3.5 ppm, i.e., $1 - Z_{back}^{\square}(3.5\ ppm)$, are plotted in Figs. 8g and h. The maps showed strong WM/GM contrasts for both cwGRASE and ssEPI that are closely resemble the convectional MTC study on the human brain (55–59). The averaged MTC(3.5 ppm) values are much higher for both GM (cwGRASE: (17.64±0.88%); ssEPI: (16.60±1.40)%, p=0.03) and WM (cwGRASE: (21.73±1.01)%; ssEPI: (18.83±1.30)%, p=0.0004) acquired with the cwGRASE compared to those by ssEPI methods (Fig. 8i).

DISCUSSION

In this study, we aimed to establish a multi-slice, high spectral resolution CEST acquisition method, and PLOF post-processing to extract and quantify both Guan and amide CEST signals in the human brain at 3T. High GuanCEST signals were observed at 3T on the human brain. Two rapid CEST acquisition schemes were compared with each other for the HSR-CEST. The ssEPI method can acquire multi-slice CEST images with higher SNR

than cwGRASE (737±379 vs. 602±327). AmideCEST signals acquired with steady-state saturation scheme, i.e., ssEPI, are lower than those obtained by the conventional cw saturation method, including cwTSE and cwGRASE (see table 1 and Fig. 8a). This result is consistent with an comparison study at 7T on the human brain, in which the steady-state amideCEST and NOE signals are lower than those acquired with pseudo steady-state CEST method (60). The Guan and amideCEST contrasts in WM/GM are also significantly different for the cwGRASE and ssEPI acquisition methods.

Traditionally, amideCEST was believed to have originated from mobile proteins (3–5). With the HSR-CEST method, we can accurately extract the amideCEST signal range using lower B_1 values at 0.3-0.4 μT. The amideCEST peak was found to be between 3 and 4 ppm with a low saturation power of 0.4 μT (Fig. 2 and Fig. 4f). This frequency range is consistent with the ranges (3.2 to 4.1 ppm) determined from high field MRI on both animal (6,24,25,31,61) and human brains (15,23,34) with B_1 values of 0.6-1 μT. From the conventional protein NMR studies, it has been established that the protein amide frequency span from 1.5 to 5 ppm with respect to the water resonance (62), which was also demonstrated on the broad amide proton peaks centered at 3.5 ppm in the egg white NMR spectrum (Fig. 2). However, it is interesting that the offset range of the brain amideCEST is far smaller than the typical protein amide proton range (2.8-4.2 ppm vs. 1.5-5 ppm). It is known that the offsets for the amide protons are much less dispersed in the intrinsically disordered proteins, the random coil structure of the folded protein, and the unfolded proteins (63–66). All these amide protons are collectively named unstructured amide protons. The chemical shift range of the unstructured amide protons was further verified using the unfolded egg white proteins with 50% w/w urea (Fig. 2). The frequency range and the center frequency of the unfolded proteins are similar to those of amideCEST measured in this study as well as the high field amideCEST studies (6,24,25,31,61), which suggests that the brain amideCEST signals mainly originate from the unstructured amide protons. This is understood since the unstructured amide protons exchange much more quickly than the structured amide protons with water upon exposure, thus having a higher CEST signal than other amide protons. This small group of amide protons detected by amideCEST can also explain the relatively low concentration of amideCEST (41.7 mM) measured in a previous study (33). The amideCEST signals from the folded protein, i.e., structured amideCEST, are not clearly visible in the Z-spectrum.

The high GuanCEST signal at 3T is consistent with the high field MRI observation, in which the GuanCEST intensity is even higher than the amideCEST intensities with specific B_1 values (GuanCEST 2.9% at 2 μT vs. amideCEST 1.87% at 1 μT)(6,24,25,31,32,61). The GuanCEST has not been well studied on 3T MRI for two reasons: Firstly, most of the previous CEST studies were performed with very few offsets and cannot easily separate the seriously overlapped Guan and amideCEST peaks. Secondly, high saturation power (around 2 μT) was implemented in most APT-weighted studies (9), which can dramatically decrease the signal at 2.28 ppm. This B_1 dependent CEST signal has been shown in a B_1-dependent study on both human brains (Fig. 4e) and the phantom results (Fig. 3d). The optimum B_1 values, 0.8 μT for the white matter (WM) and 1.0 μT for the gray matter (GM) were determined for amideCEST with cwTSE. They are close to the previously observed values (0.8-1 μT) on high magnetic fields (24,33,60). The optimum B_1 value is 0.6 μT for the

GuanCEST in WM, identical to the value determined in the CrCrossBSA phantom (Fig. 3d), while the optimum B_1 value is 1.0 μT for the GM GuanCEST. Once the saturation B_1 passes the optimum value, the CEST signals decrease dramatically due to the MTC scaling, which has been well explained previously (16,39). The GuanCEST signal at the high field include both protein ArgCEST signal and CrCEST signal (7,8). At 3T MRI, the CrCEST can still contribute to the GuanCEST signal as the exchange rate of the CrCEST was established to be less than 400 s^{-1} by the latest study (33). The exact contribution of CrCEST needs further validations with knockout animal models at 3T (8). Nonetheless, the CrCEST can dominate the GuanCEST peak with low pH values, at which the CrCEST exchange rate can drop to the slow-exchanging region, as shown in a recent study in the rat model of stroke. (26) Both asparagine and glutamine side-chain amide protons also impact the CEST between 2-2.7 ppm, as demonstrated in the unfolded egg white (Fig. 2), which are usually doublet peaks separated by around 0.7 ppm (50–52). The side-chain amide signals between 2.5-3.0 ppm are expected to be much smaller than the Arg proton signal as previously recorded by the downfield MRS study (54) and CEST study at an extremely high MRI field (21.1T). (41) In the current study, contributions from asparagine and glutamine side-chain amide protons were summarized by a single peak at 2.28 ppm with GuanCEST due to a low spectral resolution at 3T. However, an additional peak should be added for the side-chain amide protons for the HSR-CEST at high MRI fields.

Between the rapid CEST schemes (Fig. 1), the cw scheme provides the highest signal as measured by both cwTSE and cwGRASE methods, particularly the amideCEST signal (Fig. 8). On the contrary, the ssEPI sequence generated much better image quality and SNR than the cwGRASE method (Fig.6). Although EPI can also be used for the cwCEST readout (14,67), the GRASE readout provides nearly optimal SNR for measuring the magnetization prepared by the preparation pulses, as demonstrated in the ASL field (68). It strikes a balance between the T_2* insensitivity of the pure TSE method and the time efficiency of pure EPI acquisition. The SNR of cwGRASE is higher than that of cwTSE (Fig. 6). Furthermore, cwGRASE can achieve a higher amide and GuanCEST signal in both WM and GM compared to those by ssEPI (Figs.8 a and b) as well as much less variation in both amide and GuanCEST signals compared to those by ssEPI (Figs. 8a and b). Therefore, the cwGRASE method is suggested for most Guan and amideCEST studies. The amideCEST maps obtained by ssEPI closely resemble those obtained by starCEST (22). Although amideCEST contrast obtained by steady-state saturation is lower than those of cw saturation scheme, steady-state CEST approaches such as starCEST method and its analog method, Golden-angle RAdial Sparse Parallel (GRASP) CEST (69–71), can be applied for studies with body CEST (72) or in patients with movement disorders such as Parkinson's disease where involuntary movements may otherwise compromise MR acquisition. Both Guan and amideCEST WM/GM contrasts heavily depends on the acquisition scheme due to the significantly different macromolecule concentrations in WM/GM, as demonstrated from the B_1-dependent CEST signal in both WM and GM by cwTSE (Fig. 4g) as well as the amide/Guan CEST maps by cwGRASE (Fig. 7a) and ssEPI (Fig. 7b). The reason for the significantly high WM/GM amideCEST contrast by ssEPI compared to cwGRASE is not clear but leads to great difficulty in modeling the steady-state CEST signal. For the same reason, the amide or GuanCEST signal cannot be directly correlated to the protein

concentration. Extracting protein concentration from the CEST signal can be achieved by the quantitative CEST (qCEST) MRI (73,74), which can correct the scaling introduced by the MTC or T_1 contrasts with the Bloch–McConnell equations or $R_{1\rho}$ theory (75–78).

In the current study, the PLOF background function was assumed with a simple linear function with a Lorentzian function, which was validated with the cross-linked BSA. However, the background function may need to be further improved for in vivo Z-spectrum due to the complicated contributions from other CEST signals, particularly the CEST signals close to water resonance with high exchange rates. The optimization of the background function can be achieved by comparing the ΔZ-spectra and maps with the downfield MRS spectra and imaging (54). Another limitation of the current study is missing the quantification of the amide and GuanCEST signals.

In summary, the current PLOF fitting approach provides a reliable background fitting over a wide frequency range, as demonstrated on phantoms, allowing extraction of both Guan and amideCEST at 3T. The extracted HSR-CEST spectrum closely resemble the downfield MRS from the exchangeable protons recorded on the human brain (54) but with a much higher spatial resolution and faster acquisition speed. Upon further optimization and validation, the developed cwGRASE acquisition method and PLOF processing method will provide a new clinical tool to extract multifaceted information, such as protein and pH mapping associated with different pathologies by using both Guan and amideCEST contrasts.

CONCLUSIONS

We have demonstrated that the Guan and amide CEST contrasts can be acquired using multi-slice, high resolution CEST MRI at 3T and accurately extracted using a PLOF processing method. The amideCEST can be attributed to the unstructured amide protons, as suggested by in vitro NMR study on egg white. High GuanCEST contrast centered at 2.28 ppm was observed in the human brain. The cwGRASE CEST method was found to provide higher amideCEST as well as robust Guan and amideCEST contrasts than ssEPI, while the ssEPI method provided better image quality. This study paves the way for simultaneous Guan and amide CEST mapping within a clinically feasible scan time.

Supplementary Material

Refer to Web version on PubMed Central for supplementary material.

ACKNOWLEDGEMENTS

The authors thank Mr. Joseph S. Gillen, Mrs. Terri Lee, Brawner, Ms. Kathleen A. Kahl, and Ms. Ivana Kusevic for experimental assistance. The National Institutes of Health supported this project through grants from the P41EB031771, R01015032, R01HL149742, R21AG074978, and S10OD021648.

Data Availability Statement

The code that supports the findings of this study will be made available at https://github.com/jiadixu/amide_GuanCEST.

References:

1. Ward K, Aletras A, Balaban RS. A new class of contrast agents for MRI based on proton chemical exchange dependent saturation transfer (CEST). J Magn Reson 2000;143(1):79–87. [PubMed: 10698648]
2. Van Zijl PC, Yadav NN. Chemical exchange saturation transfer (CEST): what is in a name and what isn't? Magn Reson Med 2011;65(4):927–948. [PubMed: 21337419]
3. Zhou J, van Zijl PCM. Chemical exchange saturation transfer imaging and spectroscopy. Progress in Nuclear Magnetic Resonance Spectroscopy 2006;48(2-3):109–136.
4. Zhou J, Tryggestad E, Wen Z, Lal B, Zhou T, Grossman R, Wang S, Yan K, Fu DX, Ford E, Tyler B, Blakeley J, Laterra J, van Zijl PC. Differentiation between glioma and radiation necrosis using molecular magnetic resonance imaging of endogenous proteins and peptides. Nat Med 2011;17(1):130–134. [PubMed: 21170048]
5. Zhou J, Payen JF, Wilson DA, Traystman RJ, van Zijl PC. Using the amide proton signals of intracellular proteins and peptides to detect pH effects in MRI. Nat Med 2003;9(8):1085–1090. [PubMed: 12872167]
6. Jin T, Wang P, Hitchens TK, Kim SG. Enhancing sensitivity of pH-weighted MRI with combination of amide and guanidyl CEST. Neuroimage 2017;157:341–350. [PubMed: 28602944]
7. Zhang XY, Xie J, Wang F, Lin EC, Xu J, Gochberg DF, Gore JC, Zu Z. Assignment of the molecular origins of CEST signals at 2 ppm in rat brain. Magn Reson Med 2017;78(3):881–887. [PubMed: 28653349]
8. Chen L, Zeng H, Xu X, Yadav NN, Cai S, Puts NA, Barker PB, Li T, Weiss RG, van Zijl PCM, Xu J. Investigation of the contribution of total creatine to the CEST Z-spectrum of brain using a knockout mouse model. NMR Biomed 2017;30(12):e3834.
9. Zhou J, Heo HY, Knutsson L, van Zijl PCM, Jiang S. APT-weighted MRI: Techniques, current neuro applications, and challenging issues. J Magn Reson Imaging 2019;50(2):347–364. [PubMed: 30663162]
10. van Zijl PCM, Lam WW, Xu J, Knutsson L, Stanisz GJ. Magnetization Transfer Contrast and Chemical Exchange Saturation Transfer MRI. Features and analysis of the field-dependent saturation spectrum. Neuroimage 2018;168:222–241. [PubMed: 28435103]
11. Cai K, Singh A, Poptani H, Li W, Yang S, Lu Y, Hariharan H, Zhou XJ, Reddy R. CEST signal at 2ppm (CEST@2ppm) from Z-spectral fitting correlates with creatine distribution in brain tumor. NMR Biomed 2015;28(1):1–8. [PubMed: 25295758]
12. Desmond KL, Moosvi F, Stanisz GJ. Mapping of amide, amine, and aliphatic peaks in the CEST spectra of murine xenografts at 7 T. Magn Reson Med 2014;71(5):1841–1853. [PubMed: 23801344]
13. Zhou IY, Wang E, Cheung JS, Zhang X, Fulci G, Sun PZ. Quantitative chemical exchange saturation transfer (CEST) MRI of glioma using Image Downsampling Expedited Adaptive Least-squares (IDEAL) fitting. Scientific Reports 2017;7(1):84. [PubMed: 28273886]
14. Mueller S, Stirnberg R, Akbey S, Ehses P, Scheffler K, Stocker T, Zaiss M. Whole brain snapshot CEST at 3T using 3D-EPI: Aiming for speed, volume, and homogeneity. Magn Reson Med 2020;84(5):2469–2483. [PubMed: 32385888]
15. Zaiss M, Schuppert M, Deshmane A, Herz K, Ehses P, Fullbier L, Lindig T, Bender B, Ernemann U, Scheffler K. Chemical exchange saturation transfer MRI contrast in the human brain at 9.4T. Neuroimage 2018;179:144–155. [PubMed: 29894826]
16. Xu JX, Chung LJ, Jin T. CEST imaging of creatine, phosphocreatine, and protein arginine residue in tissues. NMR Biomed 2022:DOI: 10.1002/nbm.4671.
17. Heo HY, Zhang Y, Jiang S, Lee DH, Zhou J. Quantitative assessment of amide proton transfer (APT) and nuclear overhauser enhancement (NOE) imaging with extrapolated semisolid magnetization transfer reference (EMR) signals: II. Comparison of three EMR models and application to human brain glioma at 3 Tesla. Magn Reson Med 2016;75(4):1630–1639. [PubMed: 26033553]
18. Heo HY, Zhang Y, Lee DH, Hong X, Zhou J. Quantitative assessment of amide proton transfer (APT) and nuclear overhauser enhancement (NOE) imaging with extrapolated semi-solid

magnetization transfer reference (EMR) signals: Application to a rat glioma model at 4.7 Tesla. Magn Reson Med 2016;75(1):137–149. [PubMed: 25753614]

19. Heo HY, Zhang Y, Burton TM, Jiang S, Zhao Y, van Zijl PCM, Leigh R, Zhou J. Improving the detection sensitivity of pH-weighted amide proton transfer MRI in acute stroke patients using extrapolated semisolid magnetization transfer reference signals. Magn Reson Med 2017;78(3):871–880. [PubMed: 28639301]
20. Foo LS, Larkin JR, Sutherland BA, Ray KJ, Yap WS, Hum YC, Lai KW, Manan HA, Sibson NR, Tee YK. Study of common quantification methods of amide proton transfer magnetic resonance imaging for ischemic stroke detection. Magn Reson Med 2021;85(4):2188–2200. [PubMed: 33107119]
21. Cui J, Afzal A, Zu Z. Comparative evaluation of polynomial and Lorentzian lineshape-fitted amine CEST imaging in acute ischemic stroke. Magn Reson Med 2022;87(2):837–849. [PubMed: 34590729]
22. Sui R, Chen L, Li Y, Huang J, Chan K, Xu X, van Zijl P, Xu J. Whole-brain amide CEST imaging at 3T with a steady-state radial MRI acquisition. Magn Reson Med 2021;86(2):893–906. [PubMed: 33772859]
23. Zaiss M, Windschuh J, Goerke S, Paech D, Meissner JE, Burth S, Kickingereder P, Wick W, Bendszus M, Schlemmer HP, Ladd ME, Bachert P, Radbruch A. Downfield-NOE-suppressed amide-CEST-MRI at 7 Tesla provides a unique contrast in human glioblastoma. Magn Reson Med 2017;77(1):196–208. [PubMed: 26845067]
24. Jin T, Wang P, Zong X, Kim S-G. MR imaging of the amide-proton transfer effect and the pH-insensitive nuclear overhauser effect at 9.4 T. Magn Reson Med 2013;69(3):760–770. [PubMed: 22577042]
25. Chen L, Cao S, Koehler RC, van Zijl PCM, Xu J. High-sensitivity CEST mapping using a spatiotemporal correlation-enhanced method. Magn Reson Med 2020;84(6):3342–3350. [PubMed: 32597519]
26. Zhou IY, Lu D, Ji Y, Wu L, Wang E, Cheung JS, Zhang XA, Sun PZ. Determination of multipool contributions to endogenous amide proton transfer effects in global ischemia with high spectral resolution in vivo chemical exchange saturation transfer MRI. Magn Reson Med 2019;81(1):645–652. [PubMed: 30058148]
27. Jin T, Kim SG. Role of chemical exchange on the relayed nuclear Overhauser enhancement signal in saturation transfer MRI. Magn Reson Med 2021;87(1):365–376. . [PubMed: 34382694]
28. Ling W, Regatte RR, Navon G, Jerschow A. Assessment of glycosaminoglycan concentration in vivo by chemical exchange-dependent saturation transfer (gagCEST). Proc Natl Acad Sci USA 2008;105(7):2266–2270. [PubMed: 18268341]
29. Xu J, Yadav NN, Bar-Shir A, Jones CK, Chan KW, Zhang J, Walczak P, McMahon MT, van Zijl PC. Variable delay multi-pulse train for fast chemical exchange saturation transfer and relayed-nuclear overhauser enhancement MRI. Magn Reson Med 2014;71(5):1798–1812. [PubMed: 23813483]
30. Zhou Y, van Zijl PCM, Xu J, Yadav NN. Mechanism and quantitative assessment of saturation transfer for water-based detection of the aliphatic protons in carbohydrate polymers. Magn Reson Med 2021;85(3):1643–1654. [PubMed: 32970889]
31. Chen L, Van zijl P, Wei Z, Lu H, Duan W, Wong PC, Li T, Xu J. Early detection of Alzheimer's disease using creatine chemical exchange saturation transfer magnetic resonance imaging. NeuroImage 2021;236:118071. [PubMed: 33878375]
32. Boyd PS, Breitling J, Korzowski A, Zaiss M, Franke VL, Mueller-Decker K, Glinka A, Ladd ME, Bachert P, Goerke S. Mapping intracellular pH in tumors using amide and guanidyl CEST-MRI at 9.4 T. Magn Reson Med 2021;87(5):2436–2452. [PubMed: 34958684]
33. Wang K, Sui R, Chen L, LI Y, Xu J. The exchange rates of amide and arginine guanidinium CEST in the mouse brain. bioRxiv 2022; DOI: 10.1101/2022.02.14.480399.
34. Zaiss M, Deshmane A, Schuppert M, Herz K, Glang F, Ehses P, Lindig T, Bender B, Ernemann U, Scheffler K. DeepCEST: 9.4 T Chemical exchange saturation transfer MRI contrast predicted from 3 T data - a proof of concept study. Magn Reson Med 2019;81(6):3901–3914. [PubMed: 30803000]

35. Rocco AG, Mollica L, Ricchiuto P, Baptista AM, Gianazza E, Eberini I. Characterization of the protein unfolding processes induced by urea and temperature. Biophys J 2008;94(6):2241–2251. [PubMed: 18065481]
36. Lim WK, Rosgen J, Englander SW. Urea, but not guanidinium, destabilizes proteins by forming hydrogen bonds to the peptide group. Proc Natl Acad Sci U S A 2009;106(8):2595–2600. [PubMed: 19196963]
37. Clark JH. Denaturation Changes in Egg Albumin with Urea, Radiation, and Heat. J Gen Physiol 1943;27(2):101–111. [PubMed: 19873373]
38. Goerke S, Zaiss M, Kunz P, Klika KD, Windschuh JD, Mogk A, Bukau B, Ladd ME, Bachert P. Signature of protein unfolding in chemical exchange saturation transfer imaging. NMR Biomed 2015;28(7):906–913. [PubMed: 26010522]
39. Chen L, Wei Z, Cai S, Li Y, Liu G, Lu H, Weiss RG, van Zijl PCM, Xu J. High-resolution creatine mapping of mouse brain at 11.7 T using non-steady-state chemical exchange saturation transfer. NMR Biomed 2019;32(11):e4168. [PubMed: 31461196]
40. Chen L, Schar M, Chan KWY, Huang J, Wei Z, Lu H, Qin Q, Weiss RG, van Zijl PCM, Xu J. In vivo imaging of phosphocreatine with artificial neural networks. Nat Commun 2020;11(1):1072. [PubMed: 32102999]
41. Zhang Y, Zu T, Liu R, Zhou J. Acquisition sequences and reconstruction methods for fast chemical exchange saturation transfer imaging. NMR Biomed 2022:e4699. [PubMed: 35067987]
42. Weigel M, Helms G, Hennig J. Investigation and modeling of magnetization transfer effects in two-dimensional multislice turbo spin echo sequences with low constant or variable flip angles at 3 T. Magn Reson Med 2010;63(1):230–234. [PubMed: 19859950]
43. Zhu H, Jones CK, van Zijl PC, Barker PB, Zhou J. Fast 3D chemical exchange saturation transfer (CEST) imaging of the human brain. Magn Reson Med 2010;64(3):638–644. [PubMed: 20632402]
44. Jones CK, Huang A, Xu J, Edden RA, Schar M, Hua J, Oskolkov N, Zaca D, Zhou J, McMahon MT, Pillai JJ, van Zijl PC. Nuclear Overhauser enhancement (NOE) imaging in the human brain at 7T. NeuroImage 2013;77C:114–124.
45. Jones CK, Polders D, Hua J, Zhu H, Hoogduin HJ, Zhou J, Luijten P, van Zijl PC. In vivo three-dimensional whole-brain pulsed steady-state chemical exchange saturation transfer at 7 T. Magn Reson Med 2012;67(6):1579–1589. [PubMed: 22083645]
46. Zhang Y, Yong X, Liu R, Tang J, Jiang H, Fu C, Wei R, Hsu YC, Sun Y, Luo B, Wu D. Whole-brain chemical exchange saturation transfer imaging with optimized turbo spin echo readout. Magn Reson Med 2020;84(3):1161–1172. [PubMed: 32011026]
47. Gai N, Turkbey EB, Nazarian S, van der Geest RJ, Liu CY, Lima JA, Bluemke DA. T1 mapping of the gadolinium-enhanced myocardium: adjustment for factors affecting interpatient comparison. Magn Reson Med 2011;65(5):1407–1415. [PubMed: 21500267]
48. Bie C, Liang Y, Zhang L, Zhao Y, Chen Y, Zhang X, He X, Song X. Motion correction of chemical exchange saturation transfer MRI series using robust principal component analysis (RPCA) and PCA. Quantitative imaging in medicine and surgery 2019;9(10):1697. [PubMed: 31728313]
49. Avants BB, Tustison N, Song G. Advanced normalization tools (ANTS). Insight j 2009;2(365):1–35.
50. Mackenzie HW, Hansen DF. A (13)C-detected (15)N double-quantum NMR experiment to probe arginine side-chain guanidinium (15)N(eta) chemical shifts. J Biomol NMR 2017;69(3):123–132. [PubMed: 29127559]
51. Toshio Y, Steven MP, Alex US, Julie DF-K, Lewis EK. NMR Pulse Schemes for the Sequence-Specific Assignment of Arginine Guanidino 15N and ‘H Chemical Shifts in Proteins. J Am Chem Soc 1995;117: 3556–3564.
52. Yoshimura Y, Oktaviani NA, Yonezawa K, Kamikubo H, Mulder FA. Unambiguous Determination of Protein Arginine Ionization States in Solution by NMR Spectroscopy. Angew Chem Int Ed Engl 2017;56(1):239–242. [PubMed: 27897362]
53. Gillian DH, Brian DS. Determination of the rotational dynamics and pH dependenceof the hydrogen exchange rates of the arginine guanidino group using NMR spectroscopy. Journal of Biomolecular NMR 1995;5:59–66. [PubMed: 22911436]

54. Považan M, Schär M, Gillen J, Barker PB. Magnetic resonance spectroscopic imaging of downfield proton resonances in the human brain at 3 T. Magn Reson Med 2021;87:1661–1672. [PubMed: 34971460]
55. Stanisz GJ, Kecojevic A, Bronskill MJ, Henkelman RM. Characterizing white matter with magnetization transfer and T(2). Magn Reson Med 1999;42(6):1128–1136. [PubMed: 10571935]
56. Schmierer K, Scaravilli F, Altmann DR, Barker GJ, Miller DH. Magnetization transfer ratio and myelin in postmortem multiple sclerosis brain. Ann Neurol 2004;56(3):407–415. [PubMed: 15349868]
57. Henkelman RM, Stanisz GJ, Graham SJ. Magnetization transfer in MRI: a review. NMR Biomed 2001;14(2):57–64. [PubMed: 11320533]
58. Henkelman RM, Huang X, Xiang QS, Stanisz GJ, Swanson SD, Bronskill MJ. Quantitative interpretation of magnetization transfer. Magn Reson Med 1993;29(6):759–766. [PubMed: 8350718]
59. Balaban RS, Ceckler TL. Magnetization transfer contrast in magnetic resonance imaging. Magnetic Resonance Quarterly 1992;8(2):116–137. [PubMed: 1622774]
60. Khlebnikov V, Geades N, Klomp DWJ, Hoogduin H, Gowland P, Mougin O. Comparison of pulsed three-dimensional CEST acquisition schemes at 7 tesla: steady state versus pseudosteady state. Magn Reson Med 2017;77(6):2280–2287. [PubMed: 27455028]
61. Roussel T, Rosenberg JT, Grant SC, Frydman L. Brain investigations of rodent disease models by chemical exchange saturation transfer at 21.1 T. NMR Biomed 2018;31(11):e3995. [PubMed: 30052292]
62. Cavanagh J, Fairbrother WJ, Palmer AG, Skelton NJ, Rance M. Protein NMR Spectroscopy Principles and Practice: Academic Press; 2006.
63. Dyson HJ, Wright PE. Equilibrium NMR studies of unfolded and partially folded proteins. Nat Struct Biol 1998;5 Suppl:499–503. [PubMed: 9665178]
64. Dyson HJ, Wright PE. Unfolded proteins and protein folding studied by NMR. Chem Rev 2004;104(8):3607–3622. [PubMed: 15303830]
65. Wishart DS, Bigam CG, Holm A, Hodges RS, Sykes BD. 1H, 13C and 15N random coil NMR chemical shifts of the common amino acids. I. Investigations of nearest-neighbor effects. J Biomol NMR 1995;5(1):67–81. [PubMed: 7881273]
66. Gibbs EB, Cook EC, Showalter SA. Application of NMR to studies of intrinsically disordered proteins. Arch Biochem Biophys 2017;628:57–70. [PubMed: 28502465]
67. Kim H, Krishnamurthy LC, Sun PZ. Demonstration of fast multi-slice quasi-steady-state chemical exchange saturation transfer (QUASS CEST) human brain imaging at 3T. Magn Reson Med 2022;87(2):810–819. [PubMed: 34590726]
68. Alsop DC, Detre JA, Golay X, Gunther M, Hendrikse J, Hernandez-Garcia L, Lu H, Macintosh BJ, Parkes LM, Smits M, van Osch MJ, Wang DJ, Wong EC, Zaharchuk G. Recommended implementation of arterial spin-labeled perfusion MRI for clinical applications: A consensus of the ISMRM perfusion study group and the European consortium for ASL in dementia. Magn Reson Med 2014;10.1002/mrm.25197.
69. Feng L, Axel L, Chandarana H, Block KT, Sodickson DK, Otazo R. XD-GRASP: Golden-angle radial MRI with reconstruction of extra motion-state dimensions using compressed sensing. Magn Reson Med 2016;75(2):775–788. [PubMed: 25809847]
70. Feng L, Grimm R, Block KT, Chandarana H, Kim S, Xu J, Axel L, Sodickson DK, Otazo R. Golden-angle radial sparse parallel MRI: combination of compressed sensing, parallel imaging, and golden-angle radial sampling for fast and flexible dynamic volumetric MRI. Magn Reson Med 2014;72(3):707–717. [PubMed: 24142845]
71. Xiang X, Ding X, Kai TB, Li F. GraspCEST: Fast Free-Breathing 3D Steady-State CEST MRI Using Golden-Angle Radial Sparse MR 2022; London, United Kingdom. p 6828.
72. Zhou Y, van Zijl PCM, Xu X, Xu J, Li Y, Chen L, Yadav NN. Magnetic resonance imaging of glycogen using its magnetic coupling with water. Proc Natl Acad Sci U S A 2020;117(6):3144–3149. [PubMed: 32001509]
73. Igarashi T, Kim H, Sun PZ. Detection of tissue pH with quantitative chemical exchange saturation transfer magnetic resonance imaging. NMR Biomed 2022:e4711. [PubMed: 35141979]

74. Zaiss M, Bachert P. Chemical exchange saturation transfer (CEST) and MR Z-spectroscopy in vivo: a review of theoretical approaches and methods. Phys Med Biol 2013;58(22):R221–269. [PubMed: 24201125]

75. Trott O, Palmer AG. R 1ρ relaxation outside of the fast-exchange limit. J Magn Reson 2002;154(1):157–160. [PubMed: 11820837]

76. Jin T, Autio J, Obata T, Kim SG. Spin-locking versus chemical exchange saturation transfer MRI for investigating chemical exchange process between water and labile metabolite protons. Magn Reson Med 2011;65(5):1448–1460. [PubMed: 21500270]

77. Zaiss M, Bachert P. Chemical exchange saturation transfer (CEST) and MR Z -spectroscopy in vivo : a review of theoretical approaches and methods. Phys Med Biol 2013;58(22):R221. [PubMed: 24201125]

78. Zaiss M, Bachert P. Exchange-dependent relaxation in the rotating frame for slow and intermediate exchange -- modeling off-resonant spin-lock and chemical exchange saturation transfer. NMR Biomed 2013;26(5):507–518. [PubMed: 23281186]

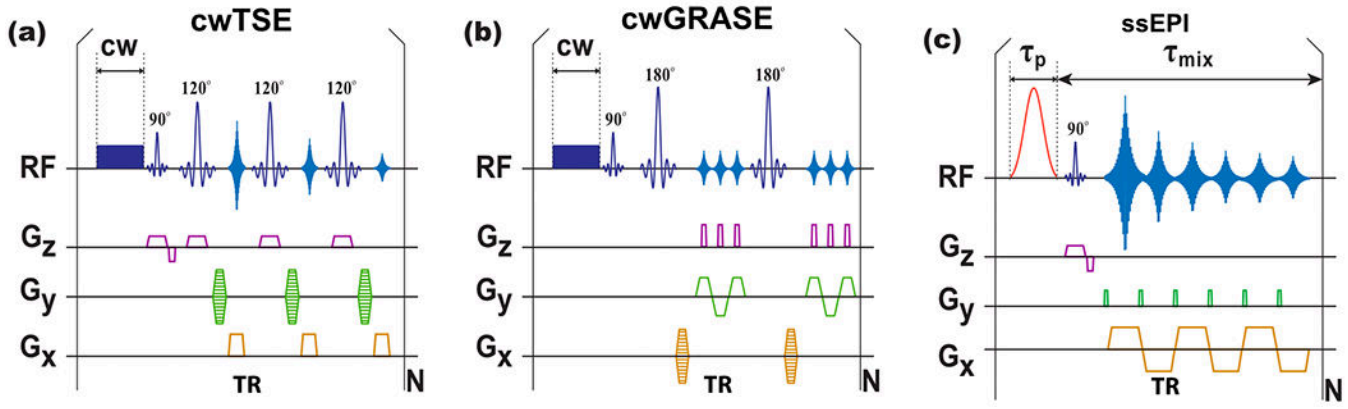

Figure 1. CEST sequences were implemented in this study.

(a) continuous wave (cw) turbo spin-echo (TSE). (b) cw GRASE. (c) steady-state EPI. τ_p is the duration of the saturation pulses and τ_{mix} is the mixing time for saturation transfer between successive saturation pulses. TR is the repetition time.

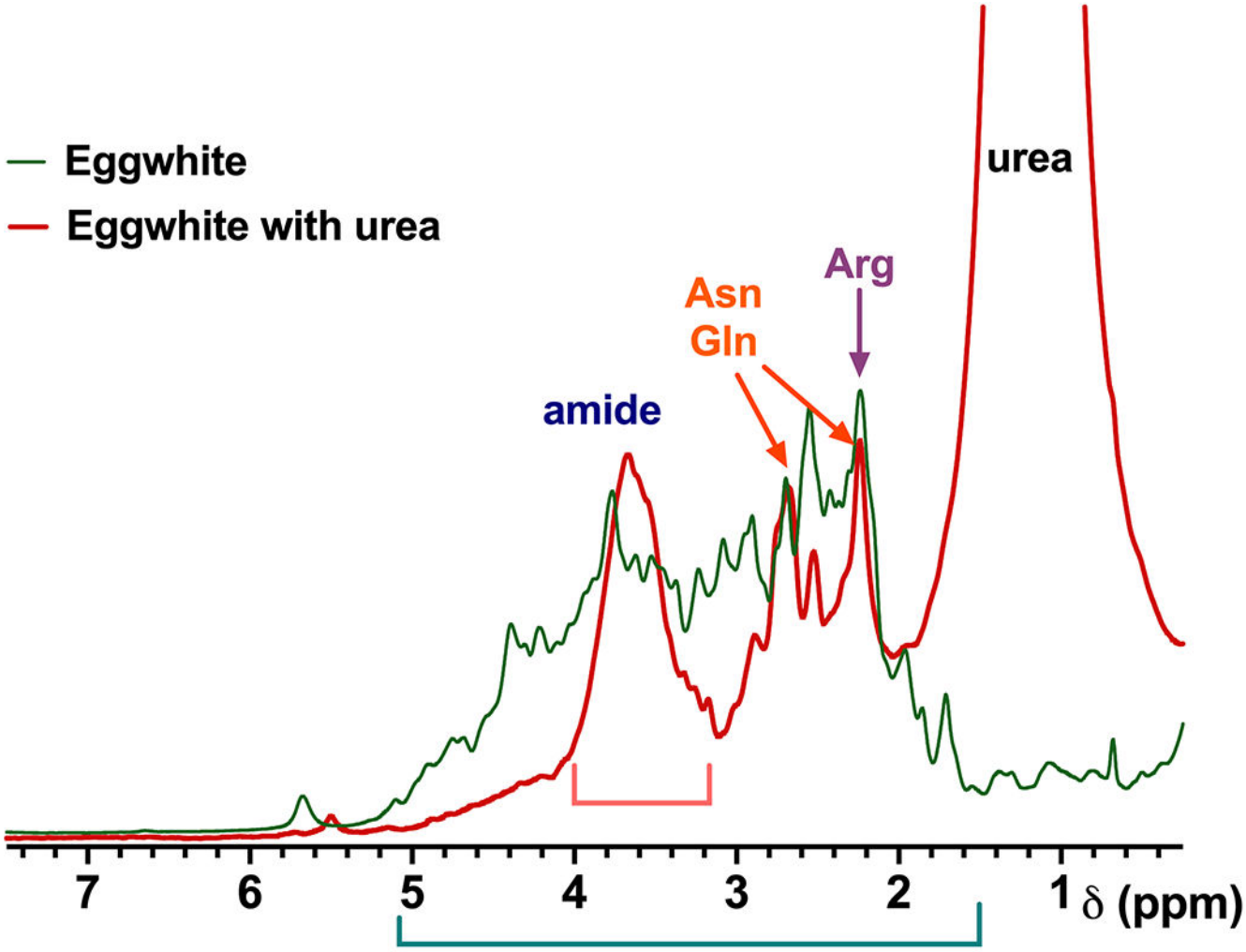

Figure 2.

Typical NMR spectra for the egg white phantoms with and without 50% urea treatment. The assignment of the peaks such as amide, asparagine (Asn) side-chain amide, glutamine (Gln) side-chain amide, and arginine (Arg) guanidinium protons are labeled. The strong urea signal is also indicated. Note that the NMR frequency is relative to the water proton resonance, which is set to zero.

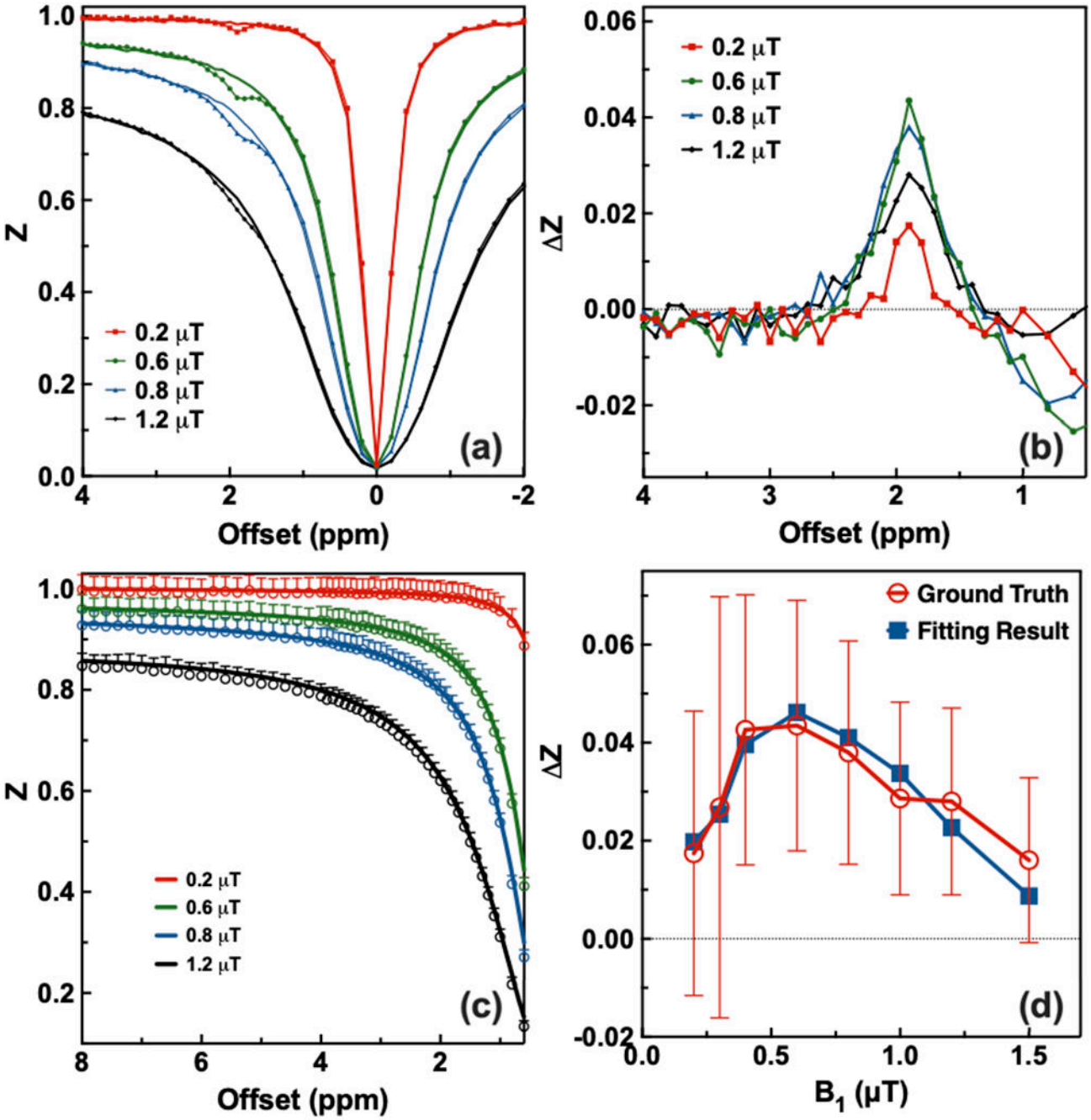

Figure 3.

Phantom validation of the PLOF method. (a) Full Z-spectra recorded for Cr with CrossBSA (solid circles) and CrossBSA alone (solid lines) using cwTSE with several typical B_1 values of 0.2 μT, 0.6 μT, 0.8 μT, and 1.2 μT. The t_{sat} was set to 1s. In CrCrossBSA Z-spectra, a clear CrCEST signal is visible at 1.9 ppm. (b) The differential Z-spectra was obtained by subtracting the two Z-spectra from CrCrossBSA and CrossBSA. (c) The typical Z-spectra of the CrossBSA alone and the PLOF background fitting (solid lines). Identical PLOF fitting parameters were used for the human brain study's fitting range and peak range. (d) The

CrCEST signal as a function of B_1 for fixed t_{sat}=1 s. The ground truth CrCEST signal (red circles) was obtained by the differential Z-spectra between the CrCrossBSA and CrossBSA at the offset of 1.9 ppm, while the CrCEST extracted by PLOF method (blue solid square) are also plotted and compared.

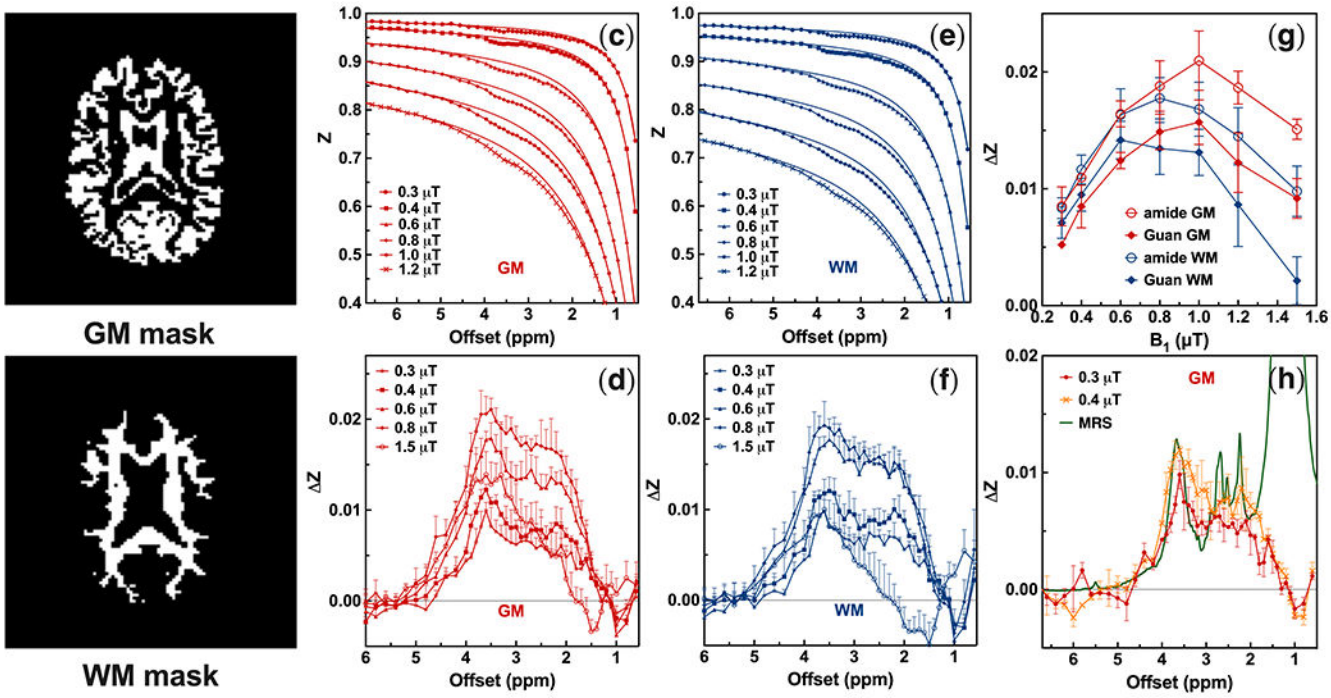

Figure 4.

Optimization of B_1 for amide/Guan CEST in GM/WM using cwTSE. The typical regions of interest, i.e., (b) GM and (c) WM, were extracted using a mask based on the T_1 map with a cut-off value of 0.7-1 s for GM and 0.5-0.7s for WM. (c-f) The averaged Z-spectrum for the GM (c, d) and WM (e, f) in the human brain (n=3) are plotted together with the PLOF background fitting of Z-spectrum (Z_{back}). (d, f) The averaged differential Z-spectrum (n=3), i.e., ΔZ spectrum, was obtained by subtracting Z_{back} by Z for (c) GM and (e) WM. (g) The averaged amide (open circle) and Guan (diamond) CEST signals (n=3) in WM (blue) and GM (red) as an function of B_1. Error bars show the standard derivation of three studies. (h) Comparison of the differential Z-spectrum in the GM acquired with B_1= 0.3 μT (red) and 0.4 μT (yellow) with the NMR spectrum of the unfolded egg white with 50% urea (green line). Guan, guanidinium; GM, gray matter; WM, white matter; TSE, turbo spin-echo; PLOF, polynomial Lorentzian line-shape fitting.

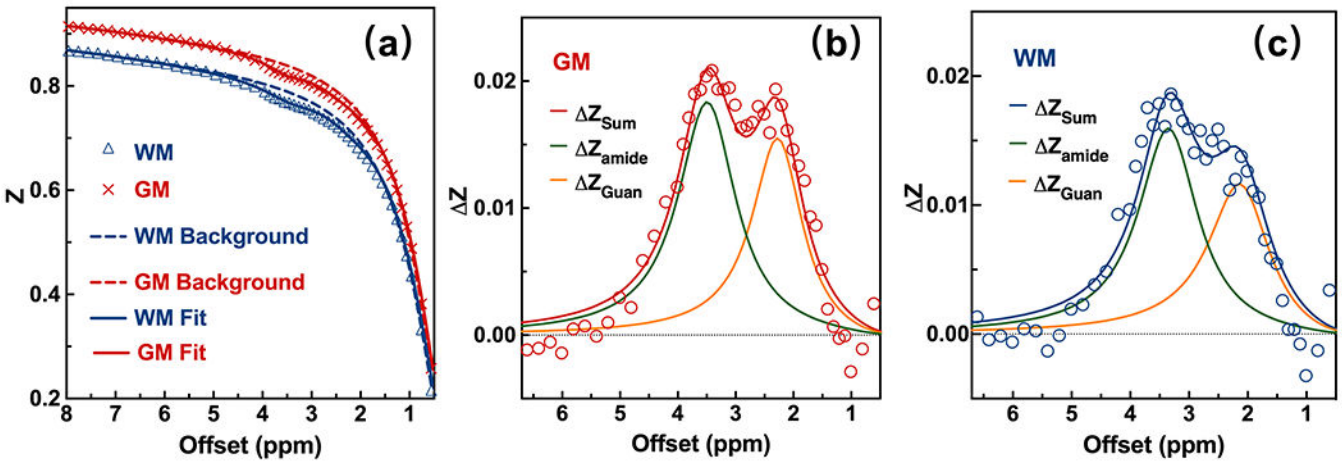

Figure 5.

Demonstration of the extraction and quantification of Guan and amide CEST with the PLOF method. (a) PLOF fitting of both background and Z-spectra in the GM (red line) and WM (blue line). The Z-spectra were extracted from the whole GM and WM, respectively. The coefficient of determination (R^2) >0.9997 for both background and the Z-spectra fitting. The Z-spectrum in the GM/WM was collected using cwTSE with B_1=0.8 μT and 1 s saturation time. (b-c) shows the typical differential Z-spectra (Z_{back}-Z), i.e., ΔZ spectrum, and the PLOF fitting results for the (b) GM and (c) WM, respectively. The two fitted amide (green line) and Guan (yellow line) CEST peaks and the sum of the two peaks are presented. Guan, guanidinium; PLOF, polynomial Lorentzian line-shape fitting; GM, gray matter; WM, white matter; TSE, turbo spin-echo.

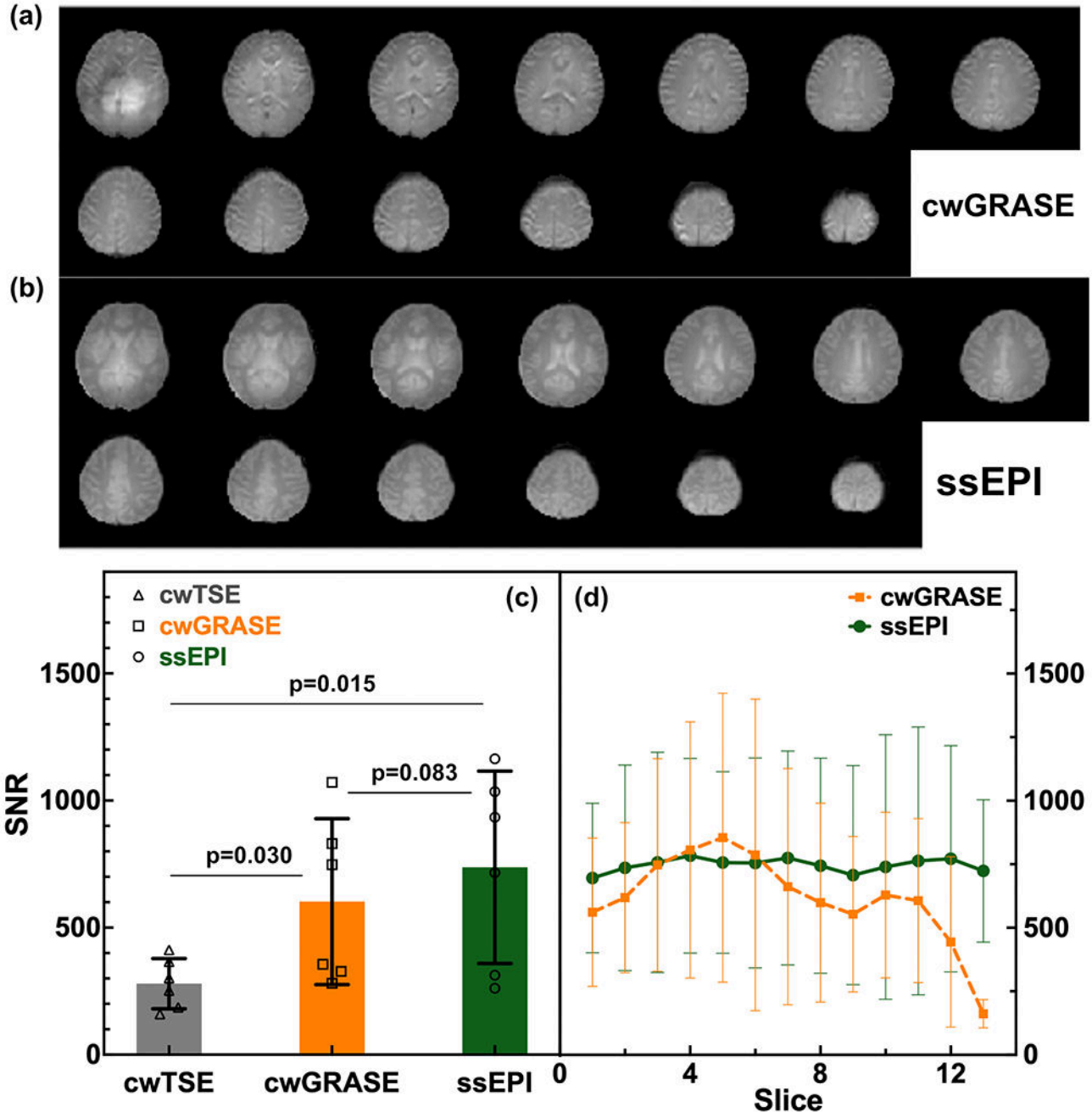

Figure 6.

Image quality comparison between cwGRASE and ssEPI. The typical M0 images for (a) cwGRASE and (b) ssEPI. (c) averaged SNR of cwTSE (n=6, gray, triangle), cwGRASE (n=6, yellow, square), and ssEPI (n=6, green, disk). Except for TSE (single slice), the SNR values of the other two methods are averaged over the total 13 slices. The error bar shows the standard derivation, and the dots represent each data point. (d) The averaged SNR of cwGRASE (yellow square) and ssEPI (green disk) for each slice. (n=6) Figs. d and c share the same y-axis for clarity. Error bars show the standard deviation of the three subjects.

GRASE, gradient- and spin-echo; EPI, echo planar imaging; TSE, turbo spin-echo; SNR, signal-to-noise ratio.

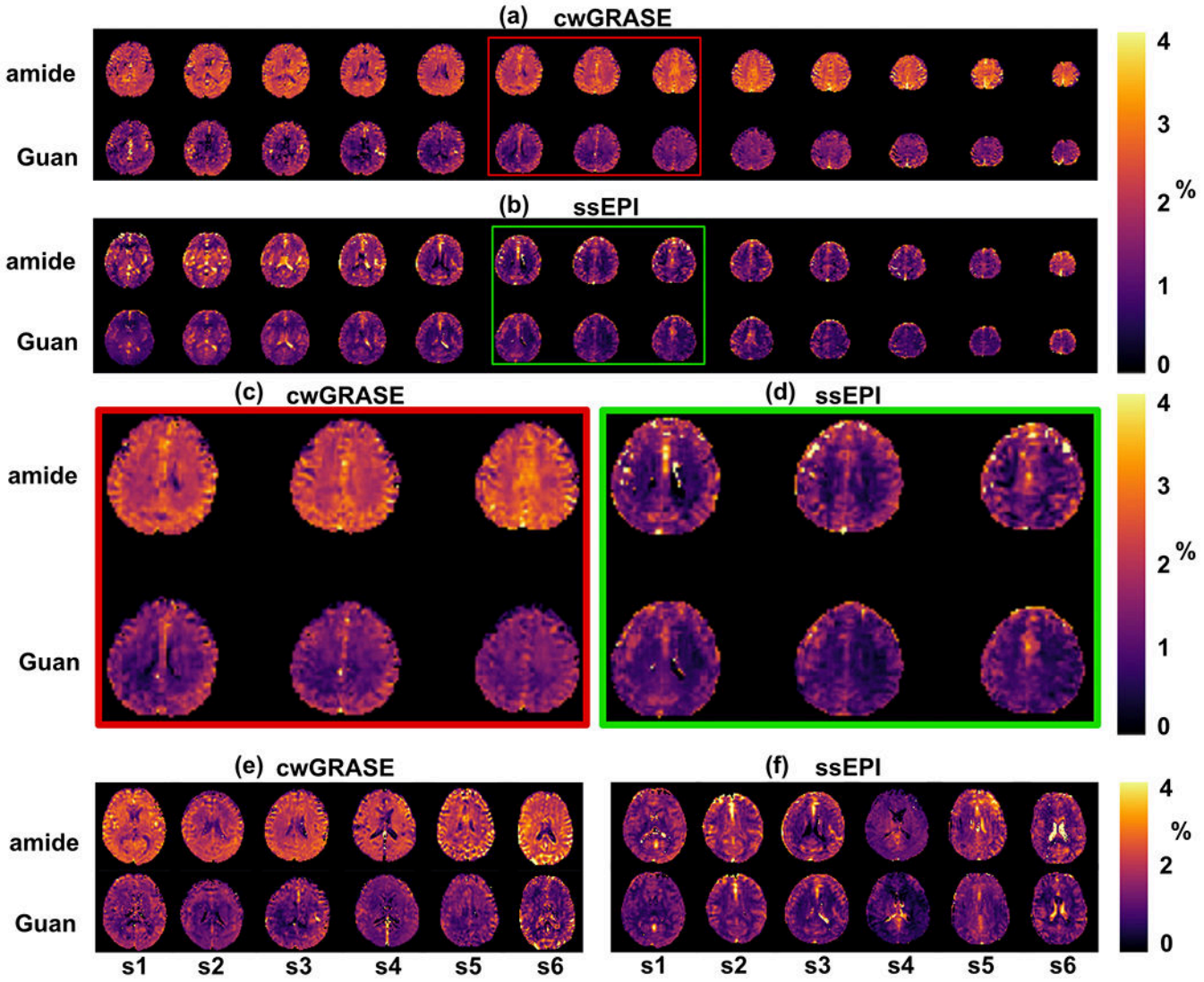

Figure 7.

Comparison of amide/Guan CEST maps collected with cwGRASE and ssEPI. (a-b) Typical amide (first line) and Guan (second line) CEST maps of (a) cwGRASE and (b) ssEPI on the same subject. (c-d) The three typical slices from the (c) cwGRASE and (d) ssEPI on the same subject, were extracted from the figures a (red rectangle) and b (green rectangle), respectively. (e-f) Single-slice amide and Guan CEST maps for six subjects (s1-s6) were acquired with the (e) cwGRASE and (f) ssEPI methods. GRASE, gradient- and spin-echo; EPI, echo planar imaging; Guan, guanidinium; GM, gray matter; WM, white matter.

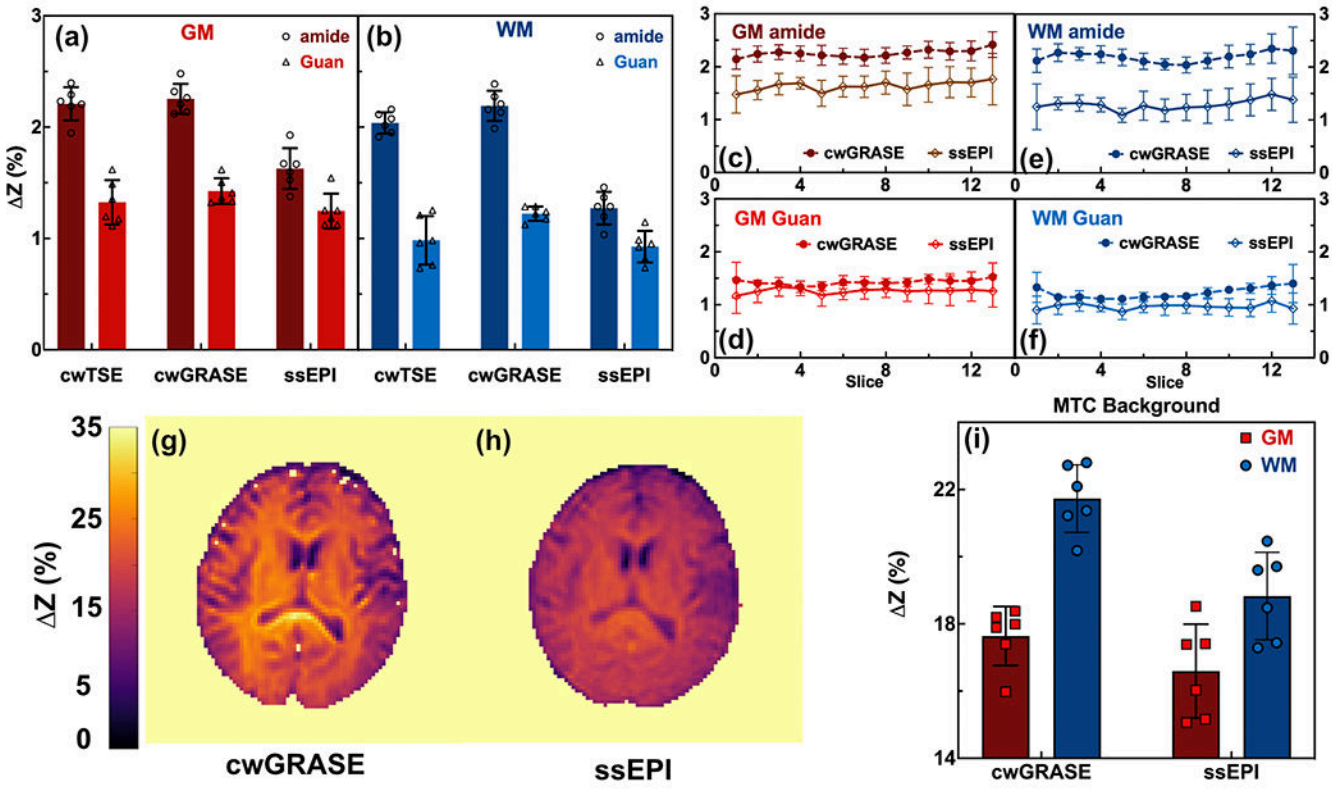

Figure 8.

Comparison of amide/Guan CEST values collected with cwGRASE and ssEPI and the MTC background. (a-b) Averaged amide (dark, circle) and Guan (light, triangle) CEST signals (n=6) extracted from three methods: cwTSE, cwGRASE, and ssEPI sequences in (a) GM, and (b) WM, respectively. (c-f) The (c,e) amide and (d,f) Guan signal for each slice in (c-d) GM, (e-f) WM acquired with EPI (solid circle, dash line), and GRASE (open diamond, dash line). Error bars show the standard derivation of all subjects (n=6). (g-h) The typical single slice MTC background at 3.5 ppm was acquired with (g) cwGRASE and (h) ssEPI, respectively. (i) Averaged MTC background signals for GM (red, square) and WM (blue, circle) acquired with cwGRASE and ssEPI (n=6). GRASE, gradient- and spin-echo; EPI, echo planar imaging; Guan, guanidinium; TSE, turbo spin-echo; GM, gray matter; WM, white matter.

Table 1:

The mean and standard deviation of the Guan and amide signals in WM/GM, with the SNR of the M0 image.

	WM		GM		SNR
	amide (%)	Guan (%)	amide (%)	Guan (%)	
cwTSE	2.04±0.10	0.98±0.22	2.21±0.15	1.33±0.20	280±99
cwGRASE	2.19±0.14	1.22±0.06	2.25±0.13	1.43±0.12	602±327
ssEPI	1.27±0.15	0.93±0.14	1.63±0.18	1.25±0.16	737±379

cwTSE, continuous wave turbo spin-echo; cwGRASE, continuous wave gradient- and spin-echo; ssEPI, steady state echo planar imaging; Guan, guanidinium; GM, gray matter; WM, white matter; SNR, signal noise ratio.